XVII. ELECTRODYNAMICS OF MEDIA[*]

Academic and Research Staff

Prof. L. J. Chu   Prof. J. I. Glaser   L. Frenkel
Prof. H. A. Haus   Prof. J. A. Kong   T. E. Sullivan
                         Prof. P. Penfield, Jr.

Graduate Students

B. L. Diamond   E. R. Kellet, Jr.   E. E. Stark, Jr.
H. Granek   E. F. McCann   L-h. Wang
P. W. Hoff   C. M. Watson

RESEARCH OBJECTIVES

1. Study of the relativistic theory of quadrupolar media has led to an asymmetric energy momentum tensor. Asymmetry of the energy momentum tensor of a closed system poses questions concerning the appropriateness of fundamental postulates underlying some formulations of electrodynamics of media. Further study will concentrate on the symmetry problem.

Also under study are problems of interaction of both electromagnetic and acoustic waves with moving media, and quantization of electromagnetic fields in material media in the presence of a charged particle. These problems are relevant to the phenomena of Brillouin scattering, Cerenkov radiation, and recent cascade shower experiments.

2. Studies of the nonlinear interactions in CO_2 lasers are concerned with cross-relaxation phenomena and amplification of cavity-dumped pulses shorter than the inverse linewidth of the CO_2 amplifier. Cross relaxation among different rotational levels will be studied in its effect of preventing hole burning and the Lamb dip. The study of short-pulse amplification will be refined through elimination of the cw background from the cavity-dumped pulse and increased power output through pulsing of the discharge.

3. Interest in quantum noise of lasers has been renewed by the expectation that new effects should be observable in a CO_2 laser near threshold. Quantum analyses are in progress to treat systems in which the noise spectrum is comparable in width with the relaxation times of the medium.

L. J. Chu, H. A. Haus, J. A. Kong, P. Penfield, Jr.

A. AN EXPERIMENTAL DETERMINATION OF CROSS RELAXATION IN CO_2

Experiments are in progress to study the relative strength of the various relaxation processes that tend to reduce the saturation of a given rotational level in the CO_2 laser, namely, the relaxation of the velocity groups across the linewidth, the relaxation of the population into the other rotational levels, and the net relaxation out of the vibrational level, dominated by vibrational-vibrational coupling. In this experiment (see Fig. XVII-1)
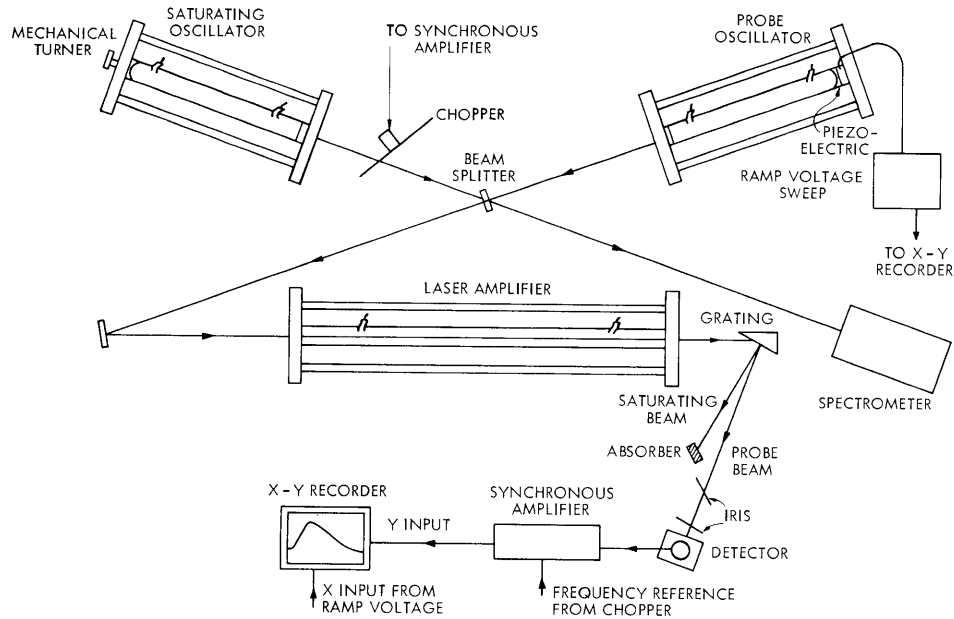

Fig. XVII-1. Schematic of experiment probing the rotational lines of CO_2.

a saturating CO_2 laser tuned to a 10. 6-μ R line is chopped (chopper in position 1) at a low frequency and modulates the population of a laser amplifier. A low-intensity beam colinear with the saturating beam is used to probe the effects of the modulation on the gain or absorption of other lasing lines of the amplifier. The probe beam is the output of a piezoelectrically tuned oscillator that can be swept across the linewidth of many P transitions. (The sweep of the piezoelectric oscillator has been calibrated in frequency by beating this laser against a fixed laser on the same line.) The probe beam is separated beyond the amplifier by a grating, and after detection is synchronously narrow-band amplified at the chopper frequency. Thus only the effect on the gain of the probe lines through modulation of the amplifier population is observed. A sample output is shown in Fig. XVII-2b for gain (discharged gas) and XVII-2c (cold gas). With the chopper in position 2, the saturating beam blocked, and the discharge on and off we can produce gain curves for the probe line, as shown in Fig. XVII-2a.

For a saturating line of R (20) used in the present experiments, all of the P transitions can be affected by the radiation field only through the rotational cross coupling, with the exception of P (22), which shares a common upper level with R (20), and P (20), which shares a common lower level. With the discharge turned on in the amplifier, the radiation field attempts to produce a Lamb dip in the upper lasing level; however, because of velocity cross relaxation, the entire level will tend to be pulled down to some extent and, because of rotational relaxation, other lines can show either the Lamb dip, or the over-all pull-down, or both. Likewise, in this case the lower levels are
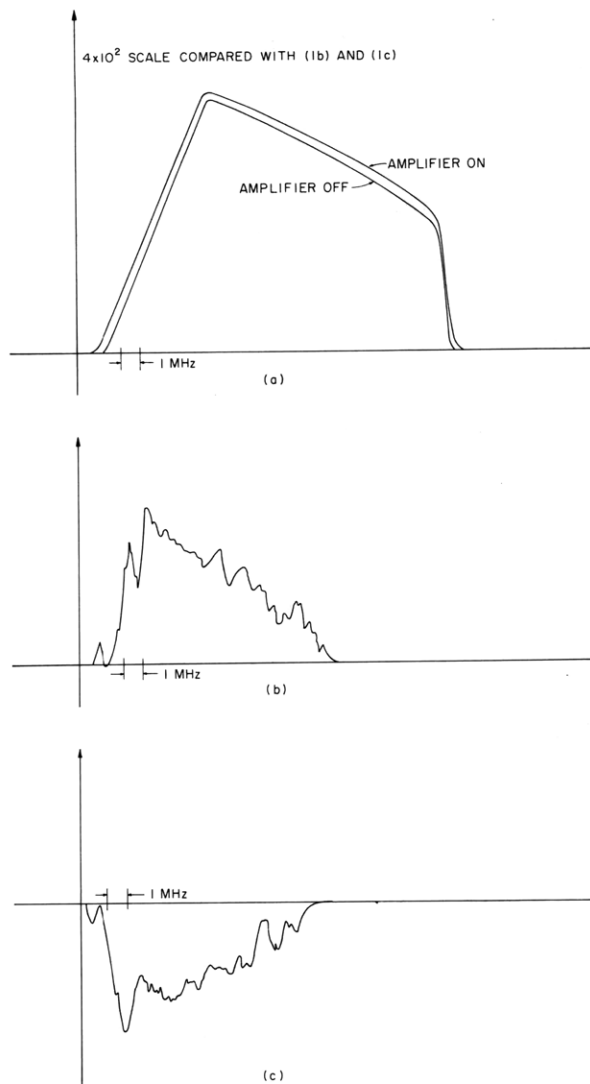
Fig. XVII-2. (a) Gain measurement of probe line P(12), 0.6 Torr N_2, 0.6 Torr CO_2.

(b) Change in absorption on probe line P(12), saturating line R(20).

(c) Gain measurement of probe line P(12), 0.6 Torr N_2, 0.6 Torr CO_2.

correspondingly filled because of the radiation field. Without the discharge, the gas in the amplifier provides absorption, and the saturating laser pumps population into the upper level, thereby reducing absorption on all levels. The process is controlled by these same parameters that depend upon the relaxation times which now, with a discharge, assume different values.

In a previous report,[1] the cross relaxation applicable to a multilevel upper

vibrational state with an entirely depleted lower vibrational state is treated. A simple extension of this approach to include the lower level includes the cases for both gain and absorption:

$$\Delta n_{\ell_2} = -\left(\frac{N_{\ell_2}^{(e)}}{g_{\ell_2}} - \frac{N_{\ell_1}^{(e)}}{g_{\ell_1}}\right)\frac{f(v)}{\gamma_2'}\left[\frac{\int W(v)\,f(v)\,dv}{\gamma_2 \tau_2'} + W(v)\right] \tag{1}$$

$$\Delta n_{j_2} = -\frac{N_{J_2}^{(e)}}{N_{\ell_2}^{(e)}}\left(\frac{N_{\ell_2}^{(e)}}{g_{\ell_2}} - \frac{N_{\ell_1}^{(e)}}{g_{\ell_1}}\right)\frac{f(v)}{\gamma_2'}\left[\frac{\int W(v)\,f(v)\,dv}{\gamma_2 \tau_2''} + W(v)\,\frac{\Lambda_2/z_2}{\left(\gamma_2 + 1/\tau_2 + \Lambda_2/z_2\right)}\right] \tag{2}$$

where

$$\frac{1}{\gamma'} = \frac{\left(\gamma + \frac{1}{\tau} + \frac{\Lambda}{z}\right)}{\left(\gamma + \frac{1}{\tau}\right)\left(\gamma + \frac{1}{\tau} + \Lambda\right)} \tag{3}$$

$$\frac{1}{\tau'} = \frac{\gamma^2 + 2\gamma\frac{\Lambda}{z} + \frac{1}{\tau}\left(\gamma + \frac{\Lambda}{z}\right) + \frac{\Lambda^2}{z}}{(\gamma+\Lambda)\left(\gamma + \frac{1}{\tau} + \frac{\Lambda}{z}\right)\tau} \tag{4}$$

$$\frac{1}{\tau''} = \frac{\frac{\Lambda}{z}\left(2\gamma + \frac{1}{\tau} + \Lambda\right)}{(\gamma+\Lambda)\left(\gamma + \frac{1}{\tau} + \frac{\Lambda}{z}\right)\tau} \tag{5}$$

with similar solutions for the lower level with a change in sign. From initial measurements we have determined that the relative pull-downs are J-independent for 0.6 Torr CO_2 and 0.6 Torr N_2.

At this pressure there was no Lamb dip; hence, we may assume that the second term in brackets in Eqs. 1 and 2 is negligible compared with the first term.

If we look at the ratio of change in gain to gain on the lasing line to that on the nonlasing lines, we get

$$\frac{\tau_2''}{\tau_2'} = \frac{\gamma^2 + \frac{\gamma}{\tau}}{\frac{\Lambda}{z}\left(2 + \frac{1}{\tau} + \Lambda\right)} + 1 = 4 \quad \text{(experimentally)}.$$

We must have $\frac{1}{\tau} \geqslant \Lambda$ in order to see this effect where γ might be smaller than either from physical arguments, and z can be calculated from equilibrium population to be approximately 14. If we take the equality between $1/\tau$ and γ, we find

$$\frac{\gamma}{2\Lambda/z} = 3 \quad \text{or} \quad \gamma \approx \frac{1}{2} \Lambda.$$

Furthermore, we know that γ cannot be too small compared with Λ because the system would not have been able to reach a new equilibrium in which the changes in the lasing level are appreciably different from changes in the other lines. An appropriate value of Λ has been given as $\sim 10^7 \ \text{sec}^{-1}$ for ~ 1 Torr from the work by Cheo.[3] Also, no Lamb dip was observed, even at 0.3 Torr CO_2 and 0.3 Torr N_2, in this amplifier experiment.

H. Granek

References

1. H. A. Haus and P. W. Hoff, "Cross Relaxation in a Multilevel System," Quarterly Progress Report No. 94, Research Laboratory of Electronics, M.I.T., July 15, 1969, pp. 80-85.

2. See graphs (Fig. V-1) in H. A. Haus and P. W. Hoff, "Effect of Cross Relaxation on Lamb Dip," Quarterly Progress Report No. 93, Research Laboratory of Electronics, M.I.T., April 15, 1969, pp. 43-48.

3. P. K. Cheo and R. L. Abrams, "Rotational Relaxation Rate of CO_2 Laser Levels," Appl. Phys. Letters 14, 47 (1969).

B. SOLUTION OF WAVEGUIDE SCATTERING PROBLEMS BY FINITE-DIFFERENCE GREEN'S DYADICS[*]

1. Introduction

This report deals with a finite-difference Green's dyadic method for the numerical calculation of the induced current distribution and equivalent circuit for time-harmonic TM modes in a two-dimensional parallel-plate waveguide impinging on a class of metallic obstacles. The class of obstacles is that with obstacle sides either parallel or perpendicular to the waveguide axis. In a previous report the finite-difference method was used to solve TE mode scattering problems in parallel-plate waveguide.[1] The TM problem involves a Green's dyadic rather than a scalar Green's function because induced currents flow in two dimensions rather than in one.

The equivalent susceptance of a transverse semidiaphragm that was computed by

---

using a 50-element approximation for the induced current distribution is 2. 06% greater than the exact value; this computation takes 1. 98 min on the IBM 360/65 computer, and costs $6. 62. This report gives a formulation of the finite-difference Green's dyadic for TM modes and the finite-difference boundary-value problem. The round-off error, sampling error, and computation costs vs number of current elements and the induced current distribution for the semidiaphragm are presented.

2. Finite-Difference Green's Dyadic

As described in a previous report, the time-harmonic Maxwell's equations can be approximated by the method of finite differences, so that each field and current component is evaluated at a different point of a cubic lattice.[2] The finite-difference Green's dyadic for TM modes in a parallel-plate waveguide is defined as the electric field solution to the finite-difference Maxwell's equations, subject to boundary conditions at the parallel plates for a discrete electric current distribution that is nonzero only at one point. The geometry of the parallel-plate waveguide and the lattice points of interest
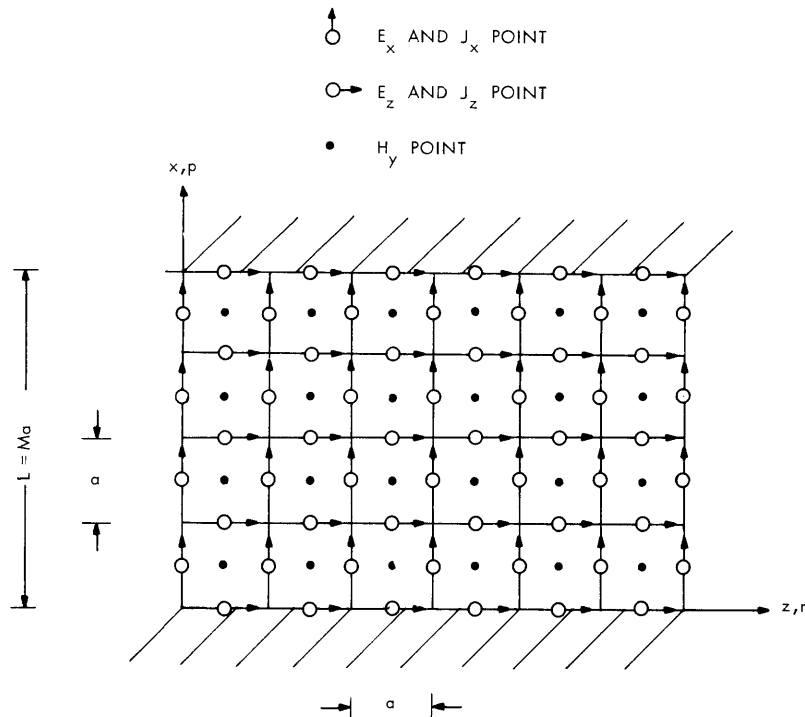

Fig. XVII-3. Geometry of lattice and parallel-plate waveguide.

is two-dimensional, and is shown in Fig. XVII-3. The coordinates x, y, and z are Cartesian, and the field and current components are independent of y. The complex magnetic field component of interest is $H_y(x, z)$ and the associated complex electric field components are $E_x(x, z)$ and $E_z(x, z)$; the complex electric current densities are given by $J_x(x, z)$ and $J_z(x, z)$. The time factor $e^{j\omega t}$, where ω is the angular frequency, will be omitted. Arrows indicate the direction of the electric field associated with each lattice point, and the numbering scheme is such that each lattice point is labeled by two integers, p and r.

$$E_x(p, r) = E_x(x, z)\bigg|_{\substack{x=(p+1/2)a \\ z=ra}}$$

$$E_z(p, r) = E_z(x, z)\bigg|_{\substack{x=pa \\ z=(p+1/2)a}}$$

$$H_y(p, r) = H_y(x, z)\bigg|_{\substack{x=(p+1/2)a \\ z=(p+1/2)a}} \tag{1}$$

The electric current density components are numbered exactly as the electric field components. The finite-difference form of Maxwell's equations is given by

$$E_z(p, r) - E_z(p+1, r) + E_x(p, r+1) - E_x(p, r) = -j\omega\mu_0 a H_y(p, r) \tag{2}$$

$$-H_y(p, r) + H_y(p, r-1) = j\omega\epsilon_0 a E_x(p, r) + a J_x(p, r) \tag{3}$$

$$-H_y(p-1, r) + H_y(p, r) = j\omega\epsilon_0 a E_z(p, r) + a J_z(p, r), \tag{4}$$

where a is the length of the side of one cell, ϵ_0 is the permittivity of free space, and μ_0 is the permeability of free space. The boundary conditions at the parallel plates are

Table XVII-1. Comparison of finite-difference TM modes and exact TM modes.

	Finite-Difference TM Mode	Exact TM Mode
H_y	$\cos\left(s\pi\left(p+\frac{1}{2}\right)/M\right) e^{-w_s r}$	$\cos(m\pi x/L) e^{-\gamma z}$
E_x	$\left((e^{w_s}-1)/j\omega\epsilon_0\right) \cos\left(s\pi\left(p+\frac{1}{2}\right)/M\right) e^{-w_s r}$	$(\gamma/j\omega\epsilon_0) \cos(m\pi x/L) e^{-\gamma z}$
E_z	$-(2\sin(s\pi/2M)/j\omega\epsilon_0) \sin(s\pi p/M) e^{-w_s r}$	$-((m\pi/L)/j\omega\epsilon_0) \sin(m\pi x/L) e^{-\gamma z}$
	$w_s = j2\sin^{-1}\left(\sqrt{(ka/2)^2 - \sin^2(s\pi/2M)}\right)$ $s = 0, 1, 2, \ldots M-1$	$\gamma = j\sqrt{k^2 - (m\pi/L)^2}$ $m = 0, 1, 2, \ldots$

obtained by choosing the origin of the lattice so that the E_z points fall along the plate boundaries.

$$E_z(p, r) = 0 \quad \text{for } p = 0 \text{ and } p = M. \tag{5}$$

The finite-difference TM modes are solutions to Eqs. 2-5 with $J_x = 0$ and $J_z = 0$. These modes are compared with the exact TM modes in Table XVII-1. Here, k is the propagation constant of free space and L = Ma. The properties of these modes have been discussed elsewhere.[3]

Green's dyadic has 4 terms, $G_{xx}, G_{xz}, G_{zx}, G_{zz}$ defined by

$$E_x(p, r) \equiv G_{xx}(p, r, p_x, r_x) j_x + G_{xz}(p, r, p_z, r_z) j_z \tag{6}$$

$$E_z(p, r) \equiv G_{zx}(p, r, p_x, r_x) j_x + G_{zz}(p, r, p_z, r_z) j_z, \tag{7}$$

where (p_x, r_x) denotes the location of an x-directed current density element of value j_x, and (p_z, r_z) denotes the location of a z-directed current density element of value j_z. The dyadic is obtained by solving Eqs. 2-5, with J_x and J_z given by

$$J_x = j_x \delta_{pp_x} \delta_{rr_x} \tag{8}$$

$$J_z = j_z \delta_{pp_z} \delta_{rr_z}, \tag{9}$$

where δ denotes a Kronecker delta function. The solutions are obtained by using the following completeness relations for the modes

$$\delta_{pp_x} = (2/M) \sum_{s=0}^{s=M-1} \epsilon_s \cos\left(s\pi\left(p+\tfrac{1}{2}\right)/M\right) \cos\left(s\pi\left(p_x+\tfrac{1}{2}\right)/M\right) \tag{10}$$

$$\delta_{pp_z} = (2/M) \sum_{s=0}^{s=M-1} \sin(s\pi p/M) \sin(s\pi p_z/M), \tag{11}$$

where $\epsilon_s = \tfrac{1}{2}$ for s = 0 and 1 for s ≠ 0.

$$G_{xx} = (-1/j\omega\epsilon_o)\delta_{pp_x}\delta_{rr_x} + \left(\frac{1}{j\omega\epsilon_o}\right)\left(\frac{2}{M}\right) \sum_{s=0}^{s=M-1} \epsilon_s \frac{\cos\left(s\pi\left(\frac{p+\frac{1}{2}}{M}\right)\right) \cos\left(s\pi\left(\frac{p_x+\frac{1}{2}}{M}\right)\right)}{2 \sinh w_s}$$

$$\cdot (2u_s(r-r_x)-u_s(r-r_x-1)-u_s(r-r_x+1)) \tag{12}$$

$$G_{xz} = \left(\frac{1}{j\omega\epsilon_0}\right)\left(\frac{2}{M}\right) \sum_{s=1}^{s=M-1} \frac{\sin\left(\frac{s\pi}{2M}\right) \cos\left(\frac{s\pi\left(p+\frac{1}{2}\right)}{M}\right) \sin\left(\frac{s\pi p_z}{M}\right)}{\sinh w_s} (u_s(r-r_z)-u_s(r-r_z-1))$$

(13)

$$G_{zx} = \left(\frac{1}{j\omega\epsilon_0}\right)\left(\frac{2}{M}\right) \sum_{s=1}^{s=M-1} \frac{\sin\left(\frac{s\pi}{2M}\right) \sin\left(\frac{s\pi p}{M}\right) \cos\left(\frac{s\pi\left(p_x+\frac{1}{2}\right)}{M}\right)}{\sinh w_s} (u_s(r-r_x)-u_s(r-r_x+1))$$

(14)

$$G_{zz} = (-1/j\omega\epsilon_0)\delta_{pp_z}\delta_{rr_z} + \left(\frac{1}{j\omega\epsilon_0}\right)\left(\frac{2}{M}\right) \sum_{s=1}^{s=M-1} \frac{2\sin^2\left(\frac{s\pi}{2M}\right) \sin\left(\frac{s\pi p}{M}\right)\sin\left(\frac{s\pi p_z}{M}\right)}{\sinh w_s} u_s(r-r_z),$$

(15)

where u_s is given by

$$u_s(r) = \exp(-w_s|r|).$$

(16)

Green's dyadic has been calculated for the x-directed current element shown in Fig. XVII-4. Here, G_{xx}/Z_0 and G_{zx}/Z_0, where Z_0 is the characteristic impedance of free space, are given for 10 different points. The frequency and dimensions have been chosen so that 2 modes are above cutoff.

3. Finite-Difference Boundary-Value Problem Solution

The finite-difference solution to the problem of determining the current distribution induced on a metallic obstacle in a parallel-plate waveguide by a TM field is obtained in three steps.

1. The current distribution on the surface of the obstacle is approximated by a set of x- and z-directed current elements having unknown amplitudes.

2. The Green's dyadic is used to compute the electric field produced at each current element location, under the assumption that each current element is excited one at a time.

3. The boundary condition that the total electric field, incident plus scattered, vanishes at each current-element location yields a set of simultaneous linear equations for the current amplitudes.

The x-directed current-element locations will be labeled by the coordinates (p_i, r_i), the current amplitudes by j_i, and the value of the incident x-directed electric field at that element by E(i), where i is an index running from 1 to N_x, the number of x-directed
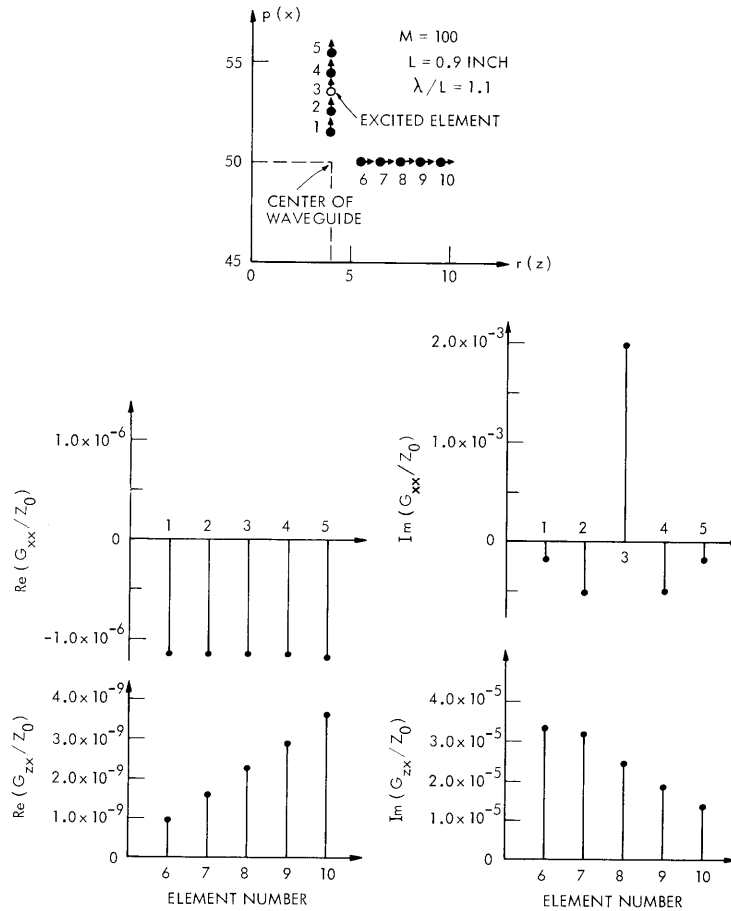
Fig. XVII-4. Green's dyadic for x-directed current element.

current elements. The same labels will be used for the corresponding z-directed variables with i running from $N_x + 1$ to $N_x + N_z$, where N_z is the number of z-directed current elements. The scattered field produced at each current element location, e(i), is then related to the current amplitudes by

$$e(i) = \sum_{k=1}^{N_x + N_z} g_{ik} j_k,$$ (17)

where

$$g_{ik} = \begin{cases} G_{xx}(p_i, r_i, p_k, r_k) & 1 \leq i, k \leq N_x \\ G_{xz}(p_i, r_i, p_k, r_k) & 1 \leq i \leq N_x; \ N_x + 1 \leq k \leq N_x + N_z \\ G_{zx}(p_i, r_i, p_k, r_k) & 1 \leq k \leq N_x; \ N_x + 1 \leq i \leq N_x + N_z \\ G_{zz}(p_i, r_i, p_k, r_k) & N_x + 1 \leq i, k, \leq N_x + N_z \end{cases}.$$ (18)

The boundary condition at the current elements is given by

$$E(i) + e(i) = 0 \qquad 1 \le i \le N_x + N_z \tag{19}$$

and yields the following set of $N_x + N_z$ simultaneous equations:

$$\sum_{k=1}^{N_x+N_z} g_{ik} j_k + e(i) = 0. \tag{20}$$

Solution to Eq. 20 for j_k can be accomplished by Gaussian elimination. The x-directed electric field of the scattered TEM (s = 0) mode can then be computed from the following expressions.

$$(\text{TEM}) \ E_x = \begin{cases} A^+ e^{-w_o r} & r > r_i \\[2mm] A^- e^{+w_o r} & r < r_i \end{cases} \tag{21}$$

where

$$A^+ = \left(\frac{1}{j\omega\epsilon_o}\right)\left(\frac{1}{M}\right) \tanh(w_o/2) \sum_{k=1}^{N_x} j_k e^{r_k w_o}$$

$$A^- = \left(\frac{1}{j\omega\epsilon_o}\right)\left(\frac{1}{M}\right) \tanh(w_o/2) \sum_{k=1}^{N_x} j_k e^{-r_k w_o}. \tag{22}$$

4. Practical Limitations of the Method

The practical limitations on the use of the method described here are sampling or discretization errors inherent in the finite-difference approximation, computation round-off error, and computation cost or time. The scattering of a TEM mode from a transverse semidiaphragm (capacitive iris) was solved in order to evaluate these limitations. The induced current distribution was obtained from Eq. 20 with N_x = 50 and N_z = 0 by Gaussian elimination, and is shown in Fig. XVII-5. The incident electric field strength was +377 V/m at r = 0, M = 100, and λ/L = 2.1, where λ is the free-space wavelength. The accuracy of the computation was tested by recomputing the scattered field at each current element location; these residual-field errors are also plotted in Fig. XVII-5 The equivalent susceptance of the transverse semidiaphragm was computed and compared with a value computed to 6-place accuracy by means of an exact series given by Collin.[4] These values are plotted against wavelength in Fig. XVII-6a. The discretization error, which is defined as the percentage difference between the computed and exact
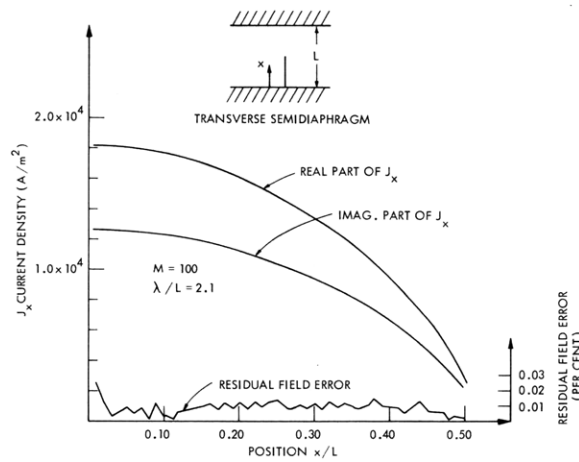
Fig. XVII-5. Induced current distribution and residual field error of transverse semidiaphragm.
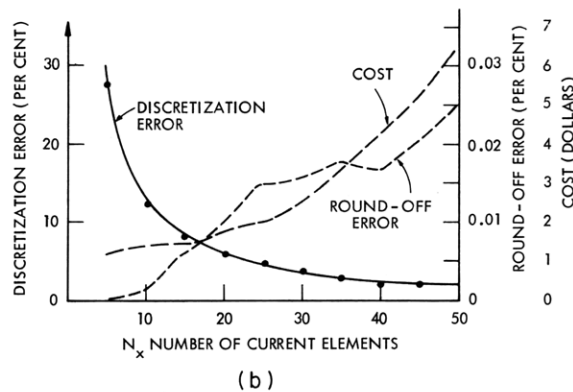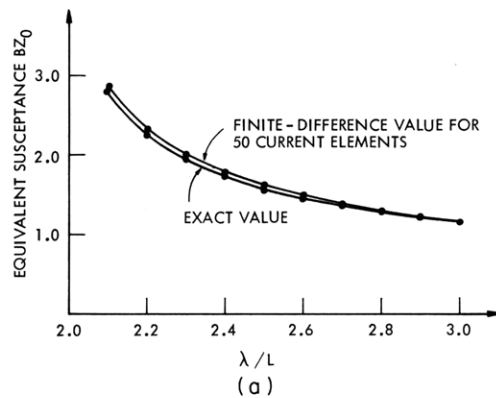

Fig. XVII-6. (a) Computed and exact equivalent susceptance of transverse semidiaphragm vs wavelength.
(b) Discretization error, round-off error and computation costs vs number of current elements.

susceptance, is plotted in Fig. XVII-6b against number of current elements. The computation costs and the round-off error, which is defined as the maximum residual-field error, are also plotted against number of current elements in Fig. XVII-6b. The cost of computation on the IBM 360/65 computer was $3.34 per 450K byte-min for central-processing unit time.

J. I. Glaser

References

1. J. I. Glaser, "Solution of Waveguide Obstacle Problems by a Finite-Difference Method," Quarterly Progress Report No. 93, Research Laboratory of Electronics, M. I. T., April 15, 1969, pp. 49-65.

2. J. I. Glaser, "Maxwell's Equations for Discrete Space," Quarterly Progress Report No. 92, Research Laboratory of Electronics, M. I. T., January 15, 1969, pp. 211-219.

3. Ibid. , pp. 218-219.

4. R. E. Collin, Field Theory of Guided Waves (McGraw-Hill Book Company, New York and London, 1960), p. 452, Prob. 10. 6.